

# Multifunctional Polymeric Phthalocyanine-Coated Carbon Nanotubes for Efficient Redox Mediators of Lithium–Sulfur Batteries

Yoonbin Kim, Won Il Kim, Hyunyoung Park, Jun Su Kim, Hyungyu Cho, Jeong Seok Yeon, Jongsoon Kim, Young-Jun Kim, Jeongyeon Lee,\* and Ho Seok Park\*

Metal phthalocyanine (Pc) complexes are considered to be promising functional organic materials owing to their tunable properties and unique  $\pi$ -electron structure. Despite these advantages, the application of polymeric metal Pc into lithium–sulfur (Li–S) batteries has yet to be explored. Herein, this work demonstrates a molecular design of multifunctional polymeric cobalt Pc with triethylene glycol linkers (TCP) that provide a redox mediating capability for the Co ion in the center of the Pc, a strong polar interaction of N atoms with Li, and the lithiophilic sites of crown ether mimicking linkers for highly efficient Li–S batteries. As verified by electrochemical and theoretical analyses, the cooperative redox mediating and lithiophilic effects of TCP coated onto multiwalled carbon nanotube (TCP/MC) are attributed to the facilitated conversion reaction kinetics of S cathodes for the high utilization efficiency of S and the inhibition of polysulfide shuttling. Consequently, the S@TCP/MC delivers high discharge capacity of 1392.8 mA h g<sup>-1</sup> and high-rate capacity of 667.9 mA h g<sup>-1</sup> at 5.0 C. Moreover, this cathode achieves a high capacity retention of 81.5% over 200 cycles, along with a high areal capacity of 6.83 mA h cm<sup>-2</sup> at 0.2 C with a high S loading of 6.6 mg cm<sup>-2</sup>.

than conventional lithium-ion (Li-ion) batteries.<sup>[1]</sup> However, the inherent limitations of currently available Li–S batteries—namely their volume expansion during the charge–discharge process, the shuttle effect of lithium polysulfides (LiPSs), and the low intrinsic conductivity of S—hamper their commercialization.<sup>[2]</sup> Extensive research is needed to develop affordable S host materials that can resolve the above-mentioned limitations, as this will enable the development of practical Li–S batteries with high energy densities and excellent cycle stabilities.<sup>[3]</sup>

Carbonaceous materials have high electrical conductivities, large surface areas, high structural stabilities, and various chemical modifications and have thus been widely studied to understand and engineer interfacial interaction and charge transfer between electrodes and electrolytes for practical Li–S batteries. Various types of carbonaceous materials have been explored, such as carbon nanotubes (CNTs),<sup>[4]</sup> graphene,<sup>[5]</sup> porous carbonaceous materials,<sup>[6]</sup> and hybrids thereof.<sup>[7]</sup> In particular, multi-walled CNTs (hereafter referred to as MCs) show unique 1D structures and sp<sup>2</sup> carbon hybridization, which endows them with outstanding electrical conductivity, mechanical durability, and chemical stability. As such, MCs are efficient

## 1. Introduction

Given by the severe global energy crisis and burgeoning demand for renewable energy, lithium–sulfur (Li–S) batteries are attracting increasing research interest as they are more cost-effective and have a higher energy density (2600 W h kg<sup>-1</sup>)

been explored, such as carbon nanotubes (CNTs),<sup>[4]</sup> graphene,<sup>[5]</sup> porous carbonaceous materials,<sup>[6]</sup> and hybrids thereof.<sup>[7]</sup> In particular, multi-walled CNTs (hereafter referred to as MCs) show unique 1D structures and sp<sup>2</sup> carbon hybridization, which endows them with outstanding electrical conductivity, mechanical durability, and chemical stability. As such, MCs are efficient

Y. Kim, W. I. Kim, J. S. Kim, H. Cho, J. S. Yeon, H. S. Park  
School of Chemical Engineering  
Sungkyunkwan University  
2066 Seobu-ro, Jangan-gu, Suwon 16419, Republic of Korea  
E-mail: phs0727@skku.edu

Y. Kim  
Convergence Research Center for Energy and Environmental Sciences  
Sungkyunkwan University  
2066 Seobu-ro, Jangan-gu, Suwon, Republic of Korea


H. Park, J. Kim  
Department of Energy Science  
Sungkyunkwan University  
2066 Seobu-ro, Jangan-gu, Suwon, Republic of Korea

H. Park, J. Kim, Y.-J. Kim, H. S. Park  
SKKU Institute of Energy Science and Technology (SIEST)  
Sungkyunkwan University  
2066 Seobu-ro, Jangan-gu, Suwon, Republic of Korea

Y.-J. Kim, H. S. Park  
SKKU Advanced Institute of Nano Technology (SAINT)  
Sungkyunkwan University  
2066 Seobu-ro, Jangan-gu, Suwon, Republic of Korea

J. Lee  
School of Fashion and Textiles  
The Hong Kong Polytechnic University, Hung Hom  
Kowloon, Hong Kong SAR, China  
E-mail: jaden-jy.lee@polyu.edu.hk

H. S. Park  
Department of Health Sciences and Technology  
Samsung Advanced Institute for Health Sciences and Technology (SAIHST)  
Sungkyunkwan University  
2066 Seobu-ro, Jangan-gu, Suwon 440-746, Republic of Korea

 The ORCID identification number(s) for the author(s) of this article can be found under <https://doi.org/10.1002/aenm.202204353>.

DOI: 10.1002/aenm.202204353

hosts of S and also act as physical barriers to prevent the loss of LiPSs, so they can be used to form Li–S batteries that have fewer limitations than non-MC-containing Li–S batteries. However, the non-polar surfaces of MCs have a weak adsorptive capacity for LiPSs,<sup>[8]</sup> which results in excessive dissolution of LiPSs and the loss of active material during the long-term cycling of Li–S batteries containing MCs, thereby decreasing their long-term cycle stability.

These above-mentioned problems can be resolved by modifying the surfaces of MCs with small organic molecules or organic polymers that can provide surfaces polarity and additional functionalities.<sup>[9]</sup> In particular, carbonaceous materials modified with metal phthalocyanines (Pcs) have great potential as effective functional organic materials for Li–S batteries owing to metal Pcs' tunable physical, optical, and electronic properties.<sup>[10]</sup> Moreover, unique 18  $\pi$ -electron aromatic core of metal Pcs can form strong  $\pi$ – $\pi$  interactions, which facilitate their attachment to the surface of MCs. Thus, for example, cobalt-centered Pcs are widely used as electrocatalysts,<sup>[11]</sup> and polymerized metal Pcs exhibit excellent coating capability, enhanced stability, and efficient catalytic metal-N<sub>4</sub> sites, making them robust electrochemical materials.<sup>[12]</sup> However, the application of metal Pcs in the field of batteries has not received much research attention. Moreover, to the best of our knowledge, there are no studies about polymeric metal Pcs coated onto MCs that function as redox mediators to enhance kinetics and Li-ion diffusivity for Li–S batteries.

Herein, we report a one-pot cyclization and polymerization process that affords novel triethylene glycol (TEG) functionalized polymeric cobalt Pcs that can be uniformly coated onto the surface of MCs to form cobalt Pc–MC conjugates, as denoted by TCP/MCs. TCP/MCs have the following five characteristics, which render them suitable for use in Li–S batteries: 1) the Co ion in the center of each Pc acts as a redox mediator for LiPS conversion and thus increases conversion reaction kinetics; 2) nitrogen (N) atoms surrounding Co donate electrons and thereby form polar interactions with Li atoms of LiPSs, which mitigates excessive LiPS dissolution; 3) oxygen atoms in TEG linkers mimic the O atoms in 12-crown-4 (a crown ether) by acting as lithiophilic sites that can host Li ions, thereby decreasing Li-ion concentration gradients; 4) electrons in the aromatic rings of Pc enhance electron mobility in MCs; and 5) the TCP coating prevents aggregation of Pcs on MCs, thereby ensuring the presence of well-dispersed active metal sites. Consequently, the resulting S@TCP/MC cathode exhibited high specific capacities of 1392.8 mA h g<sup>-1</sup> at 0.1 C, high-rate capacity of 667.9 mA h g<sup>-1</sup> at 5.0 C, and a highly reversible capacity of 861.0 mA h g<sup>-1</sup> with a capacity fading rate of 0.092% and capacity retention of 81.5% after 200 cycles. Even at a high S loading (6.6 mg cm<sup>-2</sup>), the S@TCP/MC cathode delivered a high initial capacity of 1032 mA h g<sup>-1</sup> at 0.2 C, which corresponds to an areal capacity of 6.83 mA h cm<sup>-2</sup> and underscores its potential for practical application in Li–S batteries.

## 2. Results and Discussion

Despite the environmental and economic advantages and facile tunability of organic materials,<sup>[13]</sup> their applications for Li–S batteries remains a critical challenge, due to their instability

and low electrical conductivity. In order to resolve these problems, a uniform layer of polymerized TCP was coated on the surface of an MC template to afford the high electrical conductivity of TCP/MCs.<sup>[14]</sup> **Figure 1a** is a schematic illustration about the one-pot synthesis of TCP/MCs and an S@TCP/MCs cathode. TCP/MCs were rationally designed to incorporate atomically distributed Co metal centers that serve as efficient redox mediators to accelerate the conversion reaction kinetics of S active materials. Moreover, the TEG linkers of TCP/MCs mimic 12-crown-4 by interacting favorably with Li ions, thereby facilitating their selective transport. TEG-Pn dimer, the TEG-containing bisphthalonitrile precursor of TCP/MCs, was synthesized via a nucleophilic substitution reaction from 4-nitrophthalonitrile and TEG (Figure S1, Supporting Information). The resulting crude TEG-Pn dimer was then extensively purified by washing and subsequent recrystallization from hot ethanol, which was required for obtaining a high yield of TCP/MCs (see Experimental Section for detailed procedures). The <sup>1</sup>H and <sup>13</sup>C{<sup>1</sup>H} nuclear magnetic resonance (NMR) spectra of TEG-Pn confirmed the successful construction of the desired structure (Figure S2, Supporting Information). Phthalonitrile dimers can be cyclized to Pcs, which is further polymerized.<sup>[12,15]</sup> Similarly, TEG-Pn dimer was cyclized to a Pc, which was then polymerized in the presence of appropriate amount of MCs and cobalt acetate tetrahydrate (Co(OAc)<sub>2</sub>·4H<sub>2</sub>O) to form TCP/MCs, as shown in the Figure 1a. The composition of the TCP coating, calculated as a TCP:MC weight ratio, could be controlled by adjusting the amount of MC added during the cyclization step. Unless otherwise stated, the TCP/MCs discussed herein had the composition at a TCP:MC weight ratio of 1:3.

As shown in scanning transmission electron microscopy (STEM) images of the TCP/MCs in Figure 1b, the layer of TCP is conformally coated on MCs owing to the strong  $\pi$ – $\pi$  interaction of Pcs with MCs. The amorphous TCP layer with the thickness of 2 to 3 nm on the surface of MC could be verified by the apparent lattice fringes as well as the clear outer surface of pristine MC (Figure 1c,d). Furthermore, the high-angle annular dark-field (HAADF) STEM image shown in Figure S3, Supporting Information, supported the existence of an amorphous layer with Co atoms dispersed. Despite the uniform coating of TCP, the surface of the debundled MCs is slightly roughened, which indicates the polymerization and coating of Pcs instead of homopolymerizing. Pcs can be homopolymerized in the absence of substrates with which they interact.<sup>[12]</sup> The X-ray diffraction (XRD) patterns shown in Figure S4, Supporting Information, further confirm the amorphous nature of TCP that show no distinct diffraction pattern by TCP. This is because randomly polymerized particles do not have a crystallinity while the monomeric Pcs could display typical diffraction peaks arising from self-assembly.<sup>[15]</sup> Energy dispersive spectroscopy (EDS) mapping images support the uniform dispersion of the TCP coating layers on MCs in Figure 1e, as the images show that the coating layers contain all of the elements of TCP. For comparison, the same reaction was performed in the absence of MCs, which afforded homopolymerized TCP.<sup>[15]</sup> The uniformly coated TCP layer induced uniform S incorporation to form S@TCP/MC, which was characterized using scanning electron microscopy (SEM) as shown in Figure S5, Supporting Information.

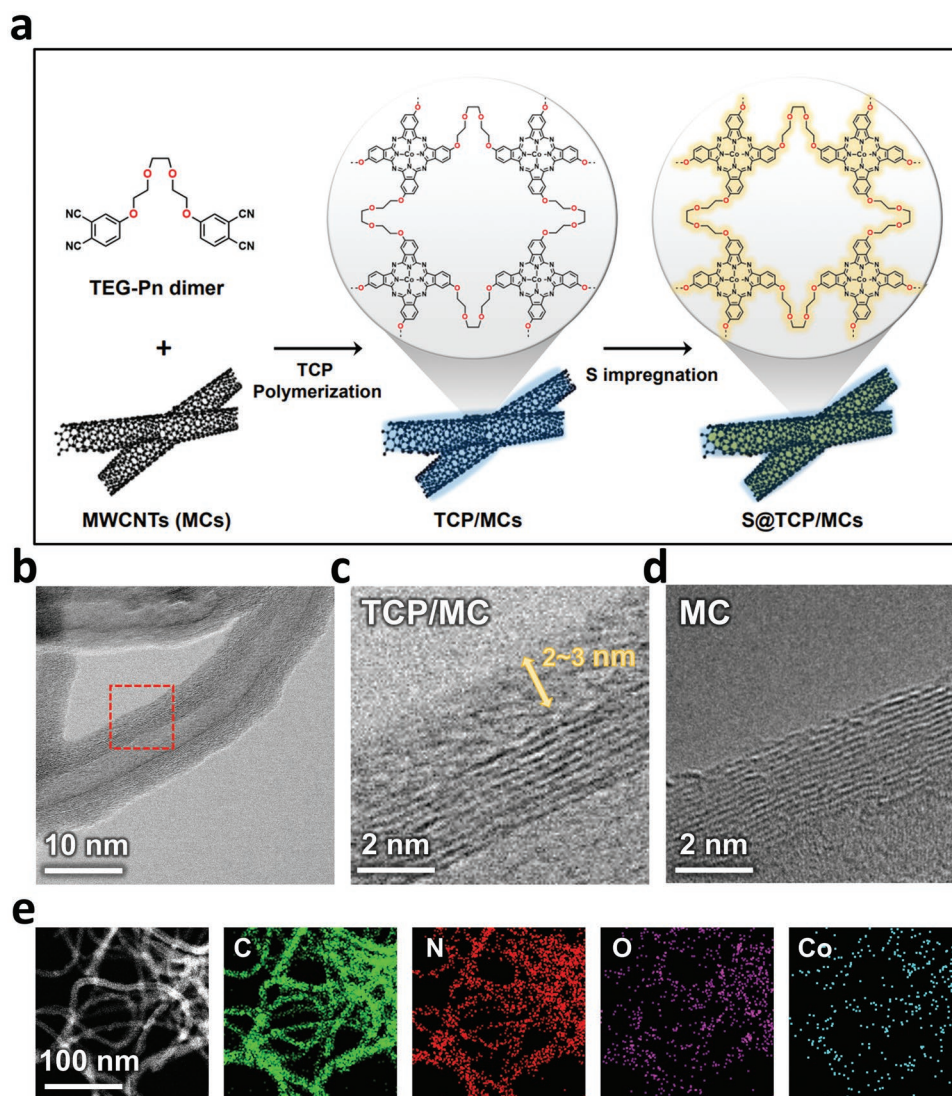


**Figure 1.** a) Schematic illustration of synthesizing the S@TCP/MCs electrode. b) STEM images of TCP/MCs. c) Boundary image of TCP/MC taken from the region marked by the dash-red rectangular in (b). d) Boundary image of pristine MC. e) Elemental mapping image corresponding to STEM image of TCP/MCs.

The electronic and chemical structures of TCP and TCP/MC were characterized using spectroscopic techniques. The UV–visible (UV–vis) spectra of TCP and TCP/MC presented in **Figure 2a** show a Q-band at 685 nm, which is a characteristic Pc peak. Due to the  $\pi$ – $\pi$  bonding between TCP and MC, TCP/MC showed shifted Q-band compared with the TCP (690 nm).<sup>[15]</sup> The formation and metal complexation of Pcs were also confirmed by Raman spectroscopy (Figure 2b). The A1g, B2g, and B1g bands located at  $\approx 688$ , 1454, and 1538  $\text{cm}^{-1}$ , respectively, correspond to isoindole C–N–C stretching, while the B1g and two A1g bands at  $\approx 752$ , 1110, and 1334  $\text{cm}^{-1}$ , respectively, represent isoindole N–M stretching.<sup>[12,15]</sup> The Fourier-transform infrared (FT-IR) spectra of TCP compounds show overlapped vibration peaks, which are assigned to C=N ( $\approx 1707 \text{ cm}^{-1}$ ), C–N ( $\approx 1610 \text{ cm}^{-1}$ ), and C–H ( $\approx 1124$ , 1064, and 753  $\text{cm}^{-1}$ ) stretches of the Pc macrocycle, and C–O stretches ( $\approx 1483$  and 1230  $\text{cm}^{-1}$ ) of the TEG linkers (Figure 2c and Figure S6, Supporting Information).<sup>[16]</sup>

X-ray photoelectron spectroscopy (XPS) was used to probe the surface chemistry and elemental composition of TCP/MCs. The full scan XPS spectrum confirms that all elements of TCP/MCs were present (Figure S7, Supporting Information). The high-resolution Co 2p spectrum in Figure 2d contains two peaks of Co<sup>2+</sup> and Co<sup>3+</sup> at 781.8 and 780.4 eV, respectively, not for Co<sup>0</sup>, which confirms the ionic coordination state of Co in TCP.<sup>[17]</sup> The coordination state of Co was also verified by the N 1s spectrum as shown in Figure 2e, which contains the characteristic peak of Co–N at 400.7 eV.<sup>[18]</sup> The high-resolution O 1s spectrum in Figure 2f shows three peaks of absorbed oxygen (532.7 and 533.7 eV) and O–C (531.6 eV), which are ascribable to the TEG linkers.<sup>[19]</sup> Moreover, the high-resolution C 1s spectrum of TCP/MCs in Figure 2g can be deconvoluted into four peaks of C–C (284.7 eV), C–N (285.4 eV), C=N (286.4 eV), and C–O (289.0 eV), which represent the Pc framework and the TEG linkers.<sup>[20]</sup>

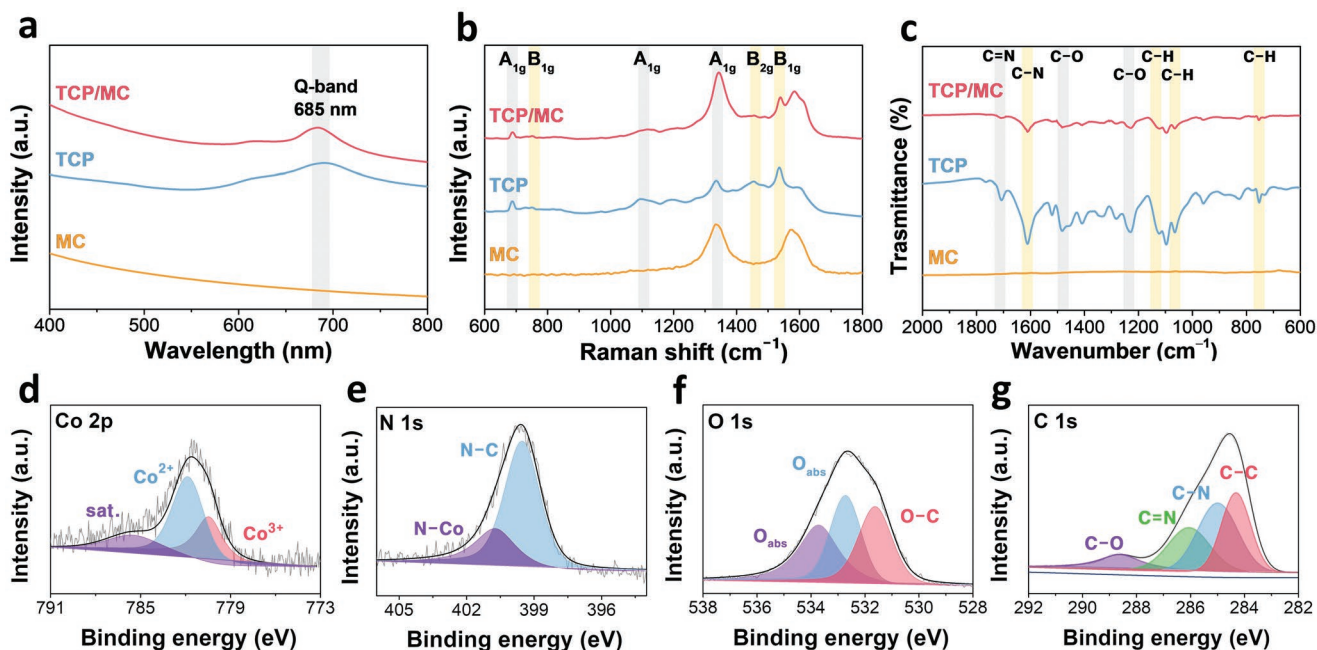


**Figure 2.** a) UV-vis b) Raman, and c) FTIR spectra of TCP/MC, TCP, and MCs. High-resolution XPS profiles of d) Co 2p, e) N 1s, f) O 1s, and g) C 1s peaks of TCP/MCs.

In order to investigate the inhibition of LiPS dissolution by TCP, an adsorption test was carried out by immersing TCP/MCs and MCs samples into a 5 mM solution of  $\text{Li}_2\text{S}_6$  (Figure 3a), which was formed by dissolving a 1:5 molar ratio of

lithium sulfide ( $\text{Li}_2\text{S}$ ) and S with 0.5 M LiTFSI in a 1:1 v/v mixture of 1,3-dioxolane and 1,2-dimethoxyethane. There was no change in the yellowish color of the  $\text{Li}_2\text{S}_6$  solution containing pristine MCs after 12 h. Furthermore, the UV-vis spectra of

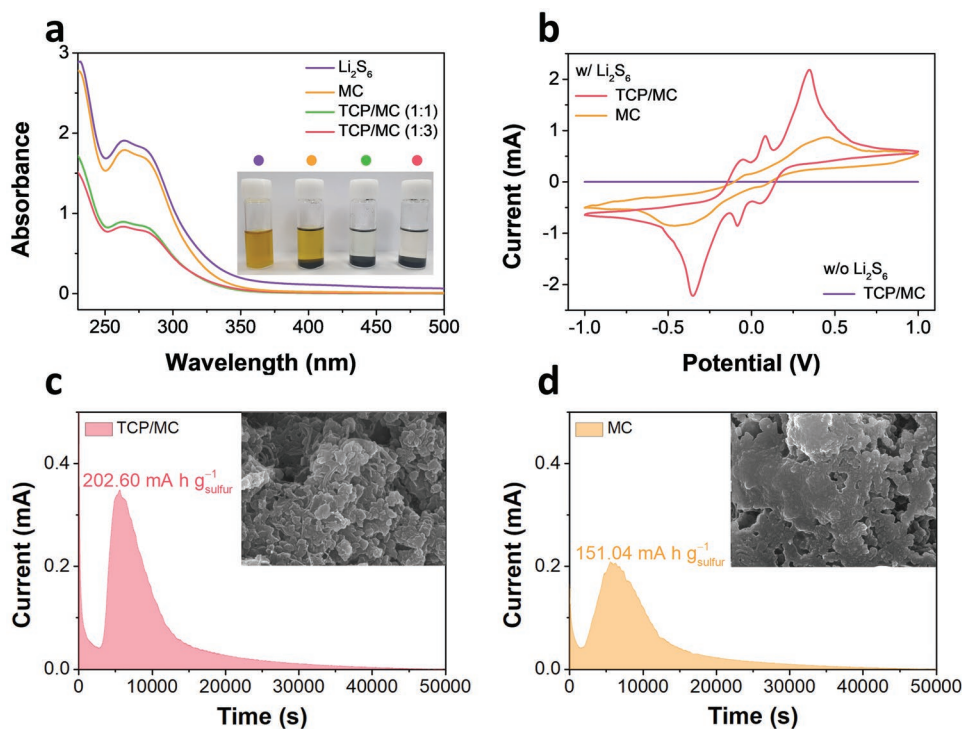


**Figure 3.** a) UV-vis spectra of  $\text{Li}_2\text{S}_6$  solution before and after adsorption (inset image: optical images of the above solutions). b) CV curves of symmetric cells containing TCP/MC in comparison to those containing MCs. c,d) Potentiostatic nucleation profiles of  $\text{Li}_2\text{S}_8$  solution on TCP/MC and MC electrodes (insets: SEM images of TCP/MC and MCs after  $\text{Li}_2\text{S}$  nucleation).

pristine MC and the  $\text{Li}_2\text{S}_6$  solution showed similar absorption intensities of peaks for hexasulfide ions (at  $\approx 260$  and  $280$  nm), indicating that the nonpolar nature of MCs allow them not to effectively adsorb LiPSs.<sup>[21]</sup> On the other hand, the  $\text{Li}_2\text{S}_6$  solutions containing TCP/MCs (with TCP:MC weight ratios of 1:1 or 1:3) turned colorless over 12 h (from yellowish), as shown in the inset in Figure 3a. In addition, the UV–vis spectra of these TCP/MCs and the  $\text{Li}_2\text{S}_6$  solution showed distinct absorption intensities at  $\approx 260$  and  $280$  nm, indicating the effective LiPS-adsorption capability of TCP. This was because unlike the non-polar surface of MCs, the polar surface of TCP can strongly immobilize LiPSs.<sup>[22]</sup> However, TCP/MCs with a TCP:MC weight ratio of 1:1 had an excessively thick coating layer of TCP that can deteriorate high electrical conductivity of MCs,<sup>[23]</sup> so its electrochemical performance was not markedly superior to that of a bare MC electrode (Figures S8 and S9, Supporting Information). By contrast, TCP/MCs with a TCP:MC weight ratio of 1:3 had an appropriate thickness of TCP coating layer. Accordingly, the electrical conductivity of TCP/MCs was enough high to achieve the superior electrochemical performance to that of a bare MC electrode. Along with the weight ratio of TCP and MC, the influence of physical features of MC used as carbonaceous templates was demonstrated by utilizing graphene as a different substrate and homopolymerized TCP without template (Figures S10 and S11, Supporting Information). Owing to the relatively large 2D surface of graphene, coating TCP over graphene was failed in that graphene was mechanically mixed with homopolymerized TCP. Consequently, S@TCP/MC outperformed other variations confirming the suitability of MC as carbon templates with facile coating ability, outstanding electrical conductivity, and structural durability.

Cyclic voltammetry (CV) curve of a TCP/MC symmetric cell in  $0.5$  M  $\text{Li}_2\text{S}_6$  electrolyte was collected to investigate the promotion of LiPS conversion kinetics (Figure 3b). The TCP/MC symmetric cell with  $\text{Li}_2\text{S}_6$  containing electrolytes exhibited distinctly separated redox pairs at  $0.05/-0.05$  V,  $-0.08/0.08$  V, and  $-0.35/0.35$  V at a scan rate of  $0.2$  mV  $\text{s}^{-1}$ , while the CV curve of a bare MC symmetric cell was distorted and unapparent. No current response of the TCP/MC symmetric cell without  $\text{Li}_2\text{S}_6$  further supports the redox feature with LiPS. Moreover, the faster conversion kinetics of LiPS was indicated by a lower overpotential and a higher redox current of the former than those of the latter. The CV profiles for three cycles at a scan rate of  $0.2$  mV  $\text{s}^{-1}$  are almost identical (Figure S12a, Supporting Information), which confirms the stable redox behavior of TCP/MC. The fast kinetics of TCP/MC for the conversion reaction of LiPSs was also demonstrated by the distinct redox peaks at various scan rates from  $0.2$  to  $2.0$  mV  $\text{s}^{-1}$ , while these peaks were absent in the CV curves of the bare MC cell (Figure S12b,c, Supporting Information). Furthermore, TCP/MC showed higher redox current compared to MC at higher scan rates from  $5.0$  to  $25.0$  mV  $\text{s}^{-1}$ , indicating the outstanding redox mediating effect on liquid state redox of LiPS conversion (Figure S13a,b).

In order to further understand the redox promoting effect of TCP on the conversion into  $\text{Li}_2\text{S}$ , the potentiostatic discharge profiles of a S-free TCP/MC electrode and S-free bare MC electrode in  $0.5$  M  $\text{Li}_2\text{S}_8$  containing electrolyte were obtained and are shown in Figure 3c,d (see Experimental section for further details). Based on Faraday's law, the  $\text{Li}_2\text{S}$  precipitation

capacities for the TCP/MC electrode and MC electrode were calculated as  $202.60$  and  $151.04$  mA h  $\text{g}_\text{s}^{-1}$ , respectively.<sup>[24]</sup> The higher capacity and current density of the TCP/MC electrode than those of the MC electrode implies the faster conversion from  $\text{Li}_2\text{S}_8$  into  $\text{Li}_2\text{S}$  as the nuclei are more accumulated on the surface of the former.<sup>[25]</sup> The precipitation morphology of  $\text{Li}_2\text{S}$  was revealed via ex situ SEM analysis of the TCP/MC and MC electrodes after  $\text{Li}_2\text{S}$  nucleation, as presented in the insets in Figure 3c,d. The ex situ SEM images of the TCP/MC electrode show that  $\text{Li}_2\text{S}$  was homogeneously deposited on the surface of the electrode. In contrast, the ex situ SEM images of the MC electrode show that  $\text{Li}_2\text{S}$  was agglomerated in the form of a thick insulating layer on the surface of the electrode.<sup>[26]</sup> These differences between the TCP/MC and MC electrodes' extent of  $\text{Li}_2\text{S}$  precipitation suggest that the Co-N<sub>4</sub> cores of TCP serve as efficient redox-mediating sites to promote LiPS conversion, which will be further characterized as below.

The electrochemical performance of the S@TCP/MC electrode was investigated in a half cell configuration with Li counter electrode in  $1.0$  LiTFSI in a 1:1 v/v mixture of 1,3-dioxolane and 1,2-dimethoxyethane with  $0.3$  LiNO<sub>3</sub>. The thermogravimetric analysis (TGA) revealed the sulfur content of the S@TCP/MC to be  $74.0$  wt% (Figure S14, Supporting Information). The CV profiles of the S@TCP/MC were measured at a scan rate of  $0.1$  mV  $\text{s}^{-1}$  in a cell voltage from  $1.7$  to  $2.8$  V and compared with those of sulfur impregnated TCP physically mixed with MC (S@mTCP/MC), and S@MC electrodes (Figure 4a). The two distinct cathodic peaks at  $\approx 2.32$  and  $2.04$  V represent the discharged species involved in solid-to-liquid phase transitions from cyclic S<sub>8</sub> to soluble long-chain LiPSs followed by liquid-solid phase transitions of long-chain LiPSs to  $\text{Li}_2\text{S}_2/\text{Li}_2\text{S}$ . Conversely, the anodic peaks at  $\approx 2.35$  and  $2.39$  V correspond to the formation of charged species involved in the reverse oxidation reactions.<sup>[27]</sup> Compared with the CV curves of the S@TCP/MC electrode, those of the MC electrode showed weaker current densities and peaks, indicating sluggish redox kinetics. In particular, the overpotential of the S@TCP/MC electrode was lower than that of the S@mTCP/MC, as shown in inset of Figure 4a. This finding confirms the importance of the polymerized TCP acting as a redox mediating host material. The CV curves of the S@TCP/MC electrode for the initial three cycles show the inevitable dissolution of LiPSs at the first cycle causing S to locate to the active sites (Figure S15, Supporting Information). Figure 4b shows the galvanostatic charge–discharge (GCD) profiles of the S@TCP/MC electrode at  $0.1$  C. The two plateaus in GCD curves are consistent with the CV profile, confirming the conversion from S<sub>8</sub> through long-chain LiPSs into  $\text{Li}_2\text{S}_2/\text{Li}_2\text{S}$ . The S@TCP/MC electrode showed higher initial specific capacity ( $1392.8$  mA h  $\text{g}^{-1}$ ) with the lower polarization potential ( $\Delta E = 150$  mV) than those of the S@mTCP/MC ( $1240.0$  mA h  $\text{g}^{-1}$  and  $\Delta E = 168$  mV) and S@MC ( $1108.8$  mA h  $\text{g}^{-1}$  and  $\Delta E = 201$  mV), respectively.

The rate capability of the S@TCP/MC electrode was estimated to analyze the redox mediation of TCP for the fast conversion kinetics. As shown in Figure 4c, the S@TCP/MC electrode exhibited the specific capacities of  $1392.8$ ,  $1078.1$ ,  $967.9$ ,  $887.4$ ,  $827.6$ ,  $787.7$ ,  $732.7$ , and  $667.9$  mA h  $\text{g}^{-1}$  at  $0.1$ ,  $0.2$ ,  $0.5$ ,  $1.0$ ,  $2.0$ ,  $3.0$ ,  $4.0$ , and  $5.0$  C, respectively. Even at a high rate of  $5.0$  C, the high capacity of  $667.9$  mA h  $\text{g}^{-1}$  was revealed in

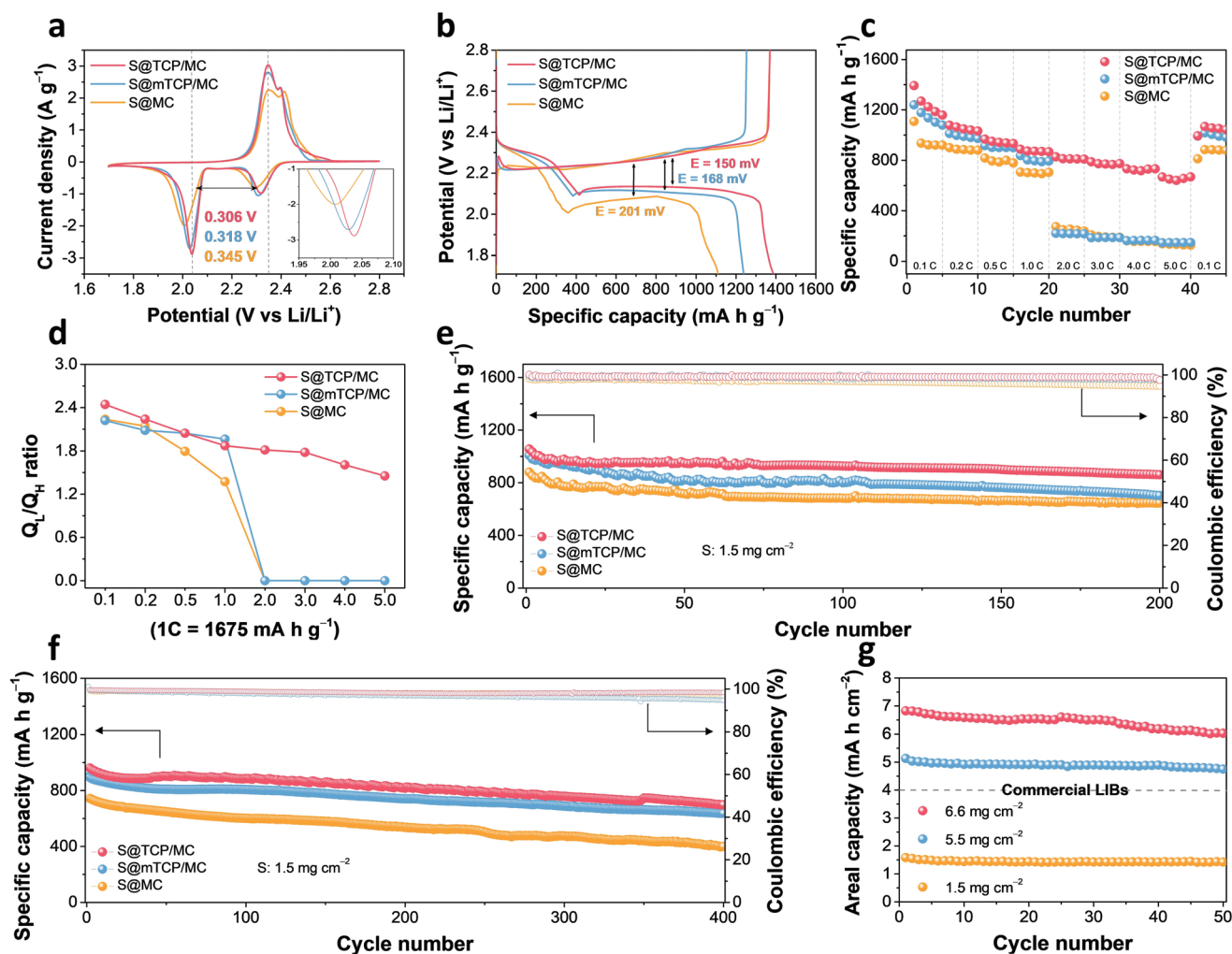


**Figure 4.** a) CV profiles at a scan rate of  $0.1 \text{ mV s}^{-1}$ , and b) galvanostatic charge–discharge curve at  $0.1 \text{ C}$  of an S@TCP/MC electrode in comparison with those of S@mTCP/MC and S@MC electrodes. c) Rate performance of S@TCP/MC, S@mTCP/MC, and S@MC electrodes at various current densities. d)  $Q_L/Q_H$  ratio at various current densities. Cycle performance at e)  $0.2 \text{ C}$ , f)  $1.0 \text{ C}$ , and g)  $0.2 \text{ C}$  with high S loadings.

the S@TCP/MC, while the capacities of the S@mTCP/MC and S@MC were drastically decayed at above  $2.0 \text{ C}$ -rates. Furthermore, two plateaus are clearly observed in the discharge profiles of the S@TCP/MC electrode, while only the first plateau is seen in the discharge profiles of the S@mTCP/MC and S@MC electrodes at high rates (Figure S16, Supporting Information). The addition of TCP to MCs, whether through coating or physical mixing, increased S utilization by increasing the capture of LiPS by electrodes. Unlike the S@mTCP/MC electrode, the S@TCP/MC electrode exhibited high reversible capacity at a high current density from  $2.0$  to  $5.0 \text{ C}$ , owing to electrons donated from the  $\pi$ – $\pi$  bonding connecting TCP and MC.<sup>[28]</sup> This behavior of the S@TCP/MC electrode was demonstrated by the polymerization of Pcs into TCP deposited onto the MC surface, owing to its efficient redox mediating effect for rapid kinetics. This result is further supported by the ratio of the low discharge plateau ( $Q_L$ ) to the high discharge plateau ( $Q_H$ ), that is,  $Q_L/Q_H$  (Figure 4d). Furthermore, the  $Q_L/Q_H$  of S@TCP/MC electrode was gradually reduced when the rates increased, while the  $Q_L/Q_H$  values of the S@mTCP/MC and

S@MC were dramatically lowered at  $2.0 \text{ C}$ -rates (Figure S16b,c, Supporting Information).

The cycle performances of the S@TCP/MC, S@mTCP/MC, and S@MC electrodes were measured (Figure 4e) to compare their electrochemical performances. The physical trapping of LiPSs by MC allowed the S@MC electrode to achieve a low initial discharge capacity of  $880.4 \text{ mA h g}^{-1}$  at  $0.2 \text{ C}$ . On the other hand, the S@TCP/MC electrode had a high initial discharge capacity of  $1056.09 \text{ mA h g}^{-1}$  with a capacity retention of  $81.5\%$  and a capacity fading rate of  $0.092\%$  over  $200$  cycles. These values were superior to those of the S@mTCP/MC electrode ( $69.74\%$  and  $0.151\%$ ) and the S@MC electrode ( $73.44\%$  and  $0.1328\%$ ), respectively. At a rate of  $1.0 \text{ C}$ , the discharge capacity of the S@TCP/MC electrode decreased from  $961.2$  to  $698.5 \text{ mA h g}^{-1}$  after  $400$  cycles, corresponding to a capacity retention of  $72.67\%$  with a capacity fading rate of  $0.068\%$ . These values were also better than those of the S@mTCP/MC electrode ( $68.39\%$  and  $0.079\%$ ) and the S@MC electrode ( $53.32\%$  and  $0.117\%$ ), respectively, as shown in Figure 4f. Moreover, S@TCP/MC showed remarkable cycle stability even at  $5.0 \text{ C}$ -rate with

low-capacity degradation of 0.055% over 800 cycles as shown in Figure S17, Supporting Information. The long-term cyclic performance of the S@TCP/MC electrode is attributable to the efficient redox mediator of the TCP and the strong interaction between the polymerized TCP and MC. In particular, it is worth noting that the electrochemical performance of S@TCP/MC outperformed the organic or polymeric host materials to date (Table S2, Supporting Information).

For the feasibility of the practical applications for Li–S batteries, the cycle performance of S@TCP/MC electrodes was examined with high S loadings (6.6 and 5.5 mg cm<sup>-2</sup>). As shown in Figure 4g, each electrode delivered high areal capacities of 6.83 and 5.13 mA h cm<sup>-2</sup> at 0.2 C, respectively. Moreover, the areal capacities of S@TCP/MC electrodes were preserved up to 6.03 and 4.75 mA h cm<sup>-2</sup>, respectively, after 50 cycles, which are higher than the areal capacity of commercial high-energy Li-ion batteries (4.0 mA h cm<sup>-2</sup>) after 50 cycles. The specific discharge capacity of 1032 mA h g<sup>-1</sup> and long-term cyclability of the S@TCP/MC electrode with the high S loading of 6.6 mg cm<sup>-2</sup> indicates the superior redox mediating effect of TCP on the high utilization efficiency of S cathodes and the inhibition of LiPS shuttling. To further validate the possibility of the practical application, pouch cell was fabricated using S@TCP/MC as a cathode (see the Experimental Section for detailed procedure). The cycle performance of the pouch cell was evaluated with electrode dimensions of 30 mm × 30 mm, which delivered an initial capacity of 1118.9 mA h g<sup>-1</sup> with a capacity retention of 81.06% for 40 cycles at 0.1 C-rate (Figure S18, Supporting Information). Also, the as-fabricated pouch cell showed good flexible nature suggesting the feasibility of S@TCP/MC for the practical application.

The electrokinetics of the S@TCP/MC electrode was analyzed to confirm the redox promoting effect of TCP on the fast conversion kinetics. Tafel plots were constructed to determine the rate-determining step of the charge–discharge process and to analyze the enhanced electrode kinetics (Figure 5a). The reduction from liquid Li<sub>2</sub>S<sub>4</sub> to solid Li<sub>2</sub>S<sub>2</sub>/Li<sub>2</sub>S, corresponding to the second cathodic peak, had the largest positive Gibbs free energy.<sup>[29]</sup> As shown in the Tafel slope of the second cathodic peak, the S@TCP/MC electrode had a lower value of ≈28.81 mV dec<sup>-1</sup> than those of the S@mTCP/MC (31.29 mV dec<sup>-1</sup>) and S@MC electrodes (52.29 mV dec<sup>-1</sup>), respectively, demonstrating that the reduction of soluble Li<sub>2</sub>S<sub>4</sub> to solid Li<sub>2</sub>S<sub>2</sub>/Li<sub>2</sub>S was more facile in the S@TCP/MC electrode than in the S@mTCP/MC and S@MC electrodes. Moreover, the Tafel slopes for the oxidation from solid Li<sub>2</sub>S<sub>2</sub>/Li<sub>2</sub>S to soluble Li<sub>2</sub>S<sub>4</sub> were 75.9, 76.62, and 77.77 mV dec<sup>-1</sup> for S@TCP/MC, S@mTCP/MC, and S@MC electrodes, respectively (Figure S19, Supporting Information), indicating the fast electrode kinetics of S@TCP/MC during a reverse process.

The interfacial charge transfer kinetics of the S@TCP/MC, S@mTCP/MC, and S@MC electrodes was analyzed collecting the Nyquist plots at open-circuit voltage (OCV), as shown in Figure 5b. A Nyquist plot consists of a semi-circle in a high-frequency region and slope of Warburg impedance in a low-frequency region.<sup>[30]</sup> The charge-transfer resistance (*R*<sub>ct</sub>) of the S@TCP/MC electrode was 30 Ω, lower than those of the S@mTCP/MC (41 Ω) and S@MC electrodes (60 Ω), respectively. Figure 5c shows the linear relationship between the real resistance (*Z'*) and inverse square root of angular speed (at ω<sup>-1/2</sup>), as obtained by the dominant equation (*Z'* = *R*<sub>s</sub> + *R*<sub>ct</sub> + σω<sup>-1/2</sup>). The value of the Warburg factor (σ) for the S@TCP/MC

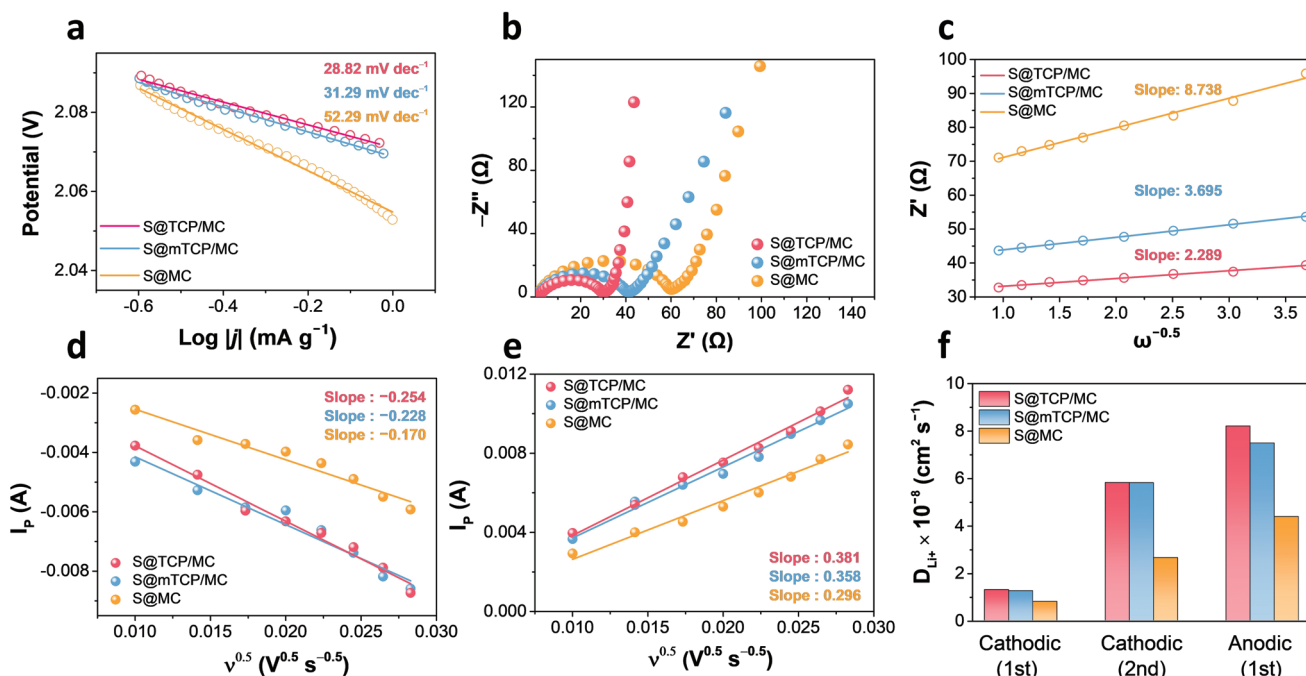


**Figure 5.** a) Tafel plots for liquid–solid reduction process (second cathodic peak). b) Nyquist plots of S@TCP/MC, S@mTCP/MC, and S@MC cathodes. c) Relationship between real resistance (*Z'*) and inverse square root of angular speed (at ω<sup>-1/2</sup>) in the low-frequency region. Plot of current values versus the square root of rates of different materials at d) second cathodic peak and e) first anodic peak in CV curves. f) Li-ion diffusion coefficients of S@TCP/MC, S@mTCP/MC, and S@MC cathodes.

electrode derived from the slope of this linear relationship was  $\approx 2.29$ , which was less than those for the S@mTCP/MC ( $\approx 3.70$ ) and S@MC ( $\approx 8.74$ ) electrodes, respectively, indicating the enhanced diffusivity of Li ions.<sup>[31]</sup> This Li-ion diffusion was further supported estimating Li-ion diffusion coefficients from the CV curves at the scan rates from 0.1 to 0.8  $\text{mV s}^{-1}$  via the Randles–Ševčík equation, as follows.

$$I_p = 2.69 \times 10^5 \times n^{1.5} \times A \times D_{\text{Li}}^{0.5} \times C_{\text{Li}} \times \nu^{0.5} \quad (1)$$

where  $I_p$  is the peak current,  $n$  is the electron transfer number,  $A$  is the electrode area,  $D_{\text{Li}}$  is the Li-ion diffusion coefficient,  $C_{\text{Li}}$  is the Li-ion concentration of the electrolyte, and  $\nu^{0.5}$  is the square root of the scan rate. As shown in the relationship between  $I_p$  and  $\nu^{0.5}$  for the second cathodic peak and the first anodic peak in Figure 5d,e, each peak corresponds to the rate-determining step of discharge and charge that dominates the overall redox reaction kinetics. The Li-ion diffusion coefficients of the S@TCP/MC electrode were found to be  $D_{\text{Li}}^{\text{cathodic (1st)}} = 1.30 \times 10^{-8}$ ,  $D_{\text{Li}}^{\text{cathodic (2nd)}} = 5.81 \times 10^{-8}$ , and  $D_{\text{Li}}^{\text{anodic (1st)}} = 8.21 \times 10^{-8}$ , respectively (Figure 5f). Interestingly, both S@TCP/MC and S@mTCP/MC samples containing TCP showed much higher Li-ion diffusion coefficients than that of pristine MC. This

result indicates that the presence of TCP was attributed to a locally lithiophilic environment that provides a uniform distribution of active sites for Li-ions, which accelerated Li-ion diffusion.<sup>[32]</sup> These results imply that the fast electrode kinetics of the S@TCP/MC electrode is associated with the fast charge transfer kinetics arising from the redox mediating TCP and the rapid Li-ion diffusion through the lithiophilic porous channels.

The above-described electrochemical kinetics and performances of the S@TCP/MC demonstrate the efficacy of incorporating cobalt Pc as a redox mediator and TEG linkers to enhance the lithiophilicity of electrodes. We next performed density functional theory (DFT) calculations to elucidate these roles of TCP. The theoretical adsorption energy ( $E_{\text{ads}}$ ) of  $\text{Li}_2\text{S}_6$  on TCP was calculated using the following equation:

$$E_{\text{ads}} = E_{\text{surface/Li}_2\text{S}_6} - (E_{\text{surface}} + E_{\text{Li}_2\text{S}_6}) \quad (2)$$

where  $E_{\text{surface/Li}_2\text{S}_6}$  is the total energy of a surface adsorbing  $\text{Li}_2\text{S}_6$ ; and  $E_{\text{surface}}$  and  $E_{\text{Li}_2\text{S}_6}$  are the total energy of the surface and  $\text{Li}_2\text{S}_6$ , respectively. A model TCP connected by four cobalt Pcs was used in DFT calculations to represent a planar form of TCP on a surface, as illustrated in Figure 6a. The  $E_{\text{ads}}$  of a LiPS molecule on a Co metal center was calculated to

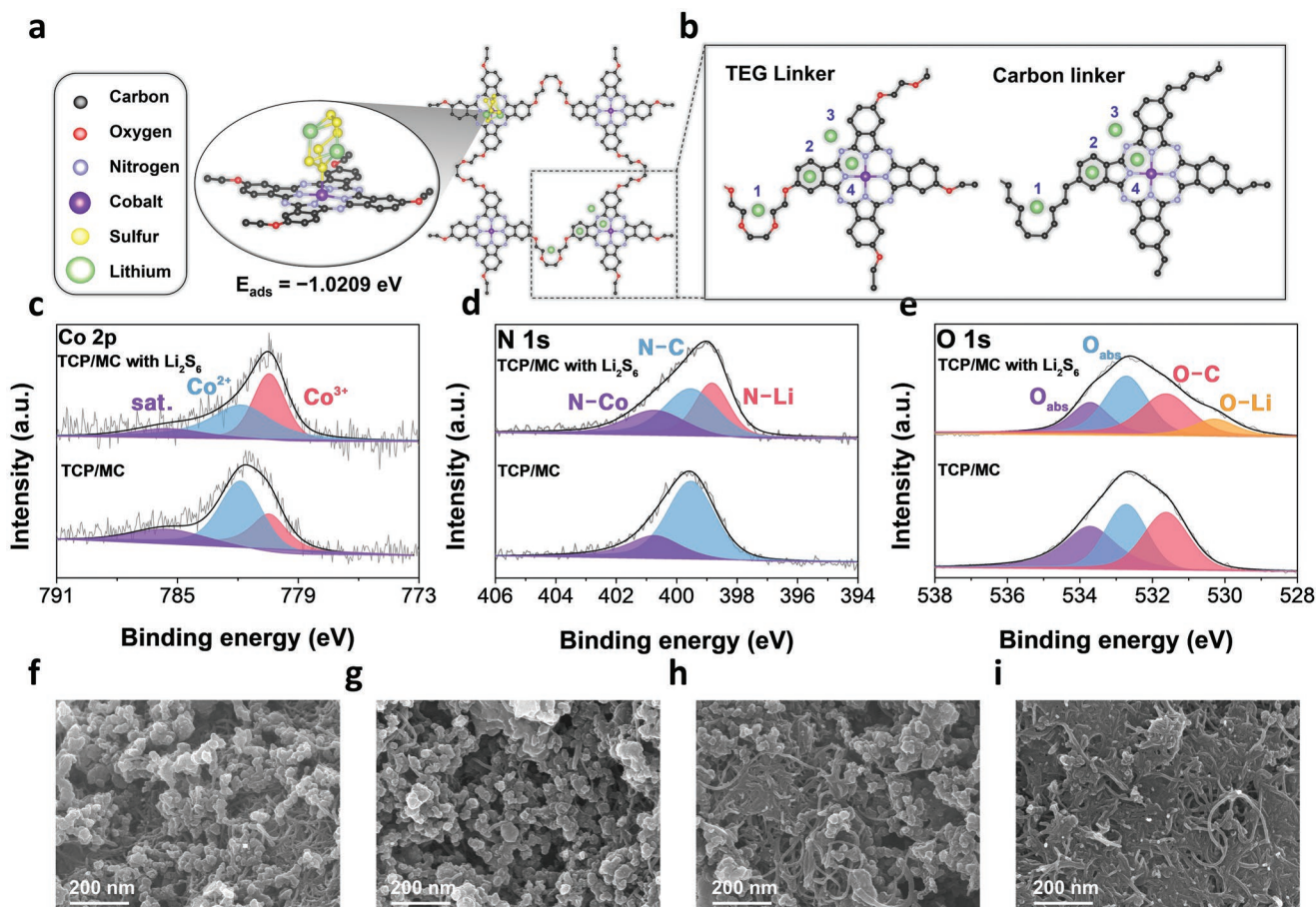


**Figure 6.** DFT calculation a) of the molecular structure of  $\text{Li}_2\text{S}_6$  adsorption on TCP and b) of the Li-ion binding energies at sites 1–4 of TCP compared with those at sites 1–4 of carbon-linker-connected CoPc. XPS profiles of c) Co 2p, d) N 1s, and e) O 1s peaks of TCP/MC before and after  $\text{Li}_2\text{S}_6$  adsorption. SEM images of an S@TCP/MC electrode f) before cycling and g) after 100 discharge–charge cycles. SEM images of MCs h) before cycling and i) after 100 discharge–charge cycles.



be  $-1.0209$  eV, which is consistent with the ability of TCP to spontaneously adsorb LiPSs, and indicates that Co atoms positioned in the core of cobalt Pc accept electrons from S atoms in  $\text{Li}_2\text{S}_6$ , thereby forming stable Co–S bonds with a bond length of  $2.38 \text{ \AA}$  (Figure S20, Supporting Information). As shown in Figure 6b, the enhanced lithiophilicity of TCP resulting from the addition of the O-rich TEG linkers was demonstrated by calculating  $E_{\text{ads}}$  for Li ions at various sites, that is, in the center of a TEG linker (site 1), on an aromatic ring (site 2), on a void (site 3), and adjacent to a Co atom (site 4). To demonstrate the effect of TEG linkers, a theoretical model with carbon linkers was used to calculate the  $E_{\text{ads}}$  at the same sites. The  $E_{\text{ads}}$  values of TCP with TEG linkers were  $-1.5560$  at site 1,  $-2.5781$  at site 2,  $-2.8035$  at site 3, and  $-1.6143$  eV at site 4, respectively, much greater than those of TCP with carbon linkers (Table S1, Supporting Information). The calculated  $E_{\text{ads}}$  for site 1 strongly supports that an electron-rich oxygen (O)-containing TEG linker provides better sites for hosting Li-ions than its analogous carbon-containing linker. The fact that the  $E_{\text{ads}}$  of other sites was also influenced by nature of the linker might be attributable to substituent effects; that is, the O atoms acted as electron donors and increased the electron density of Pc and thus also that of TCP.<sup>[12]</sup> Hence, the DFT calculations suggest that the TEG linker enhanced the lithiophilicity of TCP, which is consistent with the excellent Li-ion diffusivity of the S@TCP/MC electrode, as illustrated in Figure 5c–f. In addition, the DFT calculations suggest that Co atoms effectively trap  $\text{Li}_2\text{S}_6$  and thus function as redox mediators, while lithiophilic TEGs capture Li ions from LiPSs on active sites.

In order to support the above-mentioned DFT calculations, the XPS results about the altered surface electronic states of TCP/MC after  $\text{Li}_2\text{S}_6$  adsorption were analyzed. A TCP/MC sample was immersed into a solution of  $\text{Li}_2\text{S}_6$ , washed with solvent, and then dried in a vacuum to remove residual solvent. XPS analysis of this sample showed that its initial electronic state was different to that of a TCP/MC not exposed to a solution of  $\text{Li}_2\text{S}_6$ . Specifically, the high-resolution spectrum of Co 2p in Figure 6c illustrates that the interaction of the Co in TCP with the S in  $\text{Li}_2\text{S}_6$  was attributed to a greater proportion of  $\text{Co}^{3+}$  in the sample exposed to the solution of  $\text{Li}_2\text{S}_6$  than in the sample not exposed to the solution of  $\text{Li}_2\text{S}_6$ .<sup>[33]</sup> This instant change in the electronic state of the Co in TCP upon exposure to  $\text{Li}_2\text{S}_6$  is consistent with the DFT calculation results, where the Co metal center's adsorption of  $\text{Li}_2\text{S}_6$  result in the spontaneous formation of Co–S bonds. In addition, the high-resolution N 1s spectrum in Figure 6d contains an additional peak formed after  $\text{Li}_2\text{S}_6$  adsorption, which represents the formation of N–Li bonds at  $398.8$  eV instead of weaker N–C bonds.<sup>[34]</sup> This N–Li bonding may be a consequence of the interaction between the negatively charged N of TCP and positively charged Li comprising  $\text{Li}_2\text{S}_6$ . Moreover, the interaction of the TEG linker with Li ions was illustrated by the appearance of a peak for O–Li ( $530.2$  eV) in the high-resolution O 1s spectra, while the positions of the other peaks remained unchanged (Figure 6e).<sup>[35]</sup> These findings, taken together with the above-described electrochemical results, confirm that using cobalt Pc as a redox mediator and TEG as a linker that mimics 12-crown-4 was an effective strategy for generating a compound with enhanced LiPS conversion kinetics and Li-ion diffusivity.

To examine the microstructural and electrochemical stability of the S@TCP/MC electrode during the demanding process of continuous LiPS conversion, we compared the ex situ SEM images of the S@TCP/MC and S@MC electrodes after 100 cycles at  $0.2 \text{ C}$ , as shown in Figure 6f–i. In the initial stage, before repeated charge–discharge processes, the surface of the S@TCP/MC electrode was uniformly covered with S, while the partial surface of the MC electrode was partially covered with aggregates of S. The uniform coverage of the surface of the S@TCP/MC electrode was maintained after 100 cycles—which is attributable to the enhanced overall Li-ion binding energy of LiPSs on the active sites of the TCP/MC electrodes—whereas the surface of the MC electrode was covered with aggregated clusters of insulative  $\text{Li}_2\text{S}_2/\text{Li}_2\text{S}$ .<sup>[33b,36]</sup> These results are consistent with the morphology of  $\text{Li}_2\text{S}$  precipitation shown in the inset of Figure 3c,d and indicate that well-distributed  $\text{Li}_2\text{S}$  resulted from TCP-enhanced conversion of  $\text{Li}_2\text{S}$  to LiPSs in the charging processes. As a result, the addition of TCP not only provided various Lewis acid–base binding sites with LiPSs but also affected TCP/MC cycling performance, such that the formation of aggregated clusters containing insulative S composites was inhibited. Last, the structural stability of TCP after cycling was further examined by incorporating ex situ XPS analysis to probe elemental composition of S@TCP/MC electrodes (Figure S21, Supporting Information). Although the overall peak intensity of S@TCP/MC electrode visibly decreased as cathode-electrolyte interphase (CEI) was formed on the surface of the electrode, the dominant peak positions of Co 2p and N 1s composing the Pcs were maintained after continuous LiPS conversion. This indicated that the framework of Pcs is retained during the charge–discharge process. Similar to the XPS analysis after the immersion in LiPS solution, N–Li peak could also be found. Also, it is noteworthy that even after repetitive oxidation and reduction, a peak corresponding to the Co metal was not found, which refers to the well coordination of Co ions with the corresponding Pc metal center. This could be further supported by the corresponding N–Co peak in high resolution N 1s spectrum.

### 3. Conclusion

We have synthesized a novel polymeric cobalt Pc containing TEG linkers and coated this compound onto MCs to form TCP/MCs through a strong  $\pi$ – $\pi$  interaction. Our results showed that the TCP in TCP/MCs facilitated the absorption of LiPS and conversion reaction kinetics owing to a redox mediating capability, while the TEG linkers of TCP/MCs contained lithiophilic sites that bound Li ions. Moreover, TCP/MCs substantially enhanced the precipitation morphology of  $\text{Li}_2\text{S}$  during discharging, while also inhibiting the continuous formation of aggregated clusters containing insulative S composites during charging. As a result, the S@TCP/MC electrode provided outstanding rate performance with high initial capacities at  $0.1$  and  $5.0 \text{ C}$  ( $1392.8$  and  $667.9 \text{ mA h g}^{-1}$ , respectively). Furthermore, the S@TCP/MC electrode exhibited stable cycling performance, with a capacity fading rate of  $0.092\%$  and capacity retention of  $81.5\%$  after 200 cycles. In addition, even with a high S loading ( $6.6 \text{ mg cm}^{-2}$ ), the S@TCP/MC electrode showed an initial

capacity of 1032 mA h g<sup>-1</sup> at 0.2 C, corresponding to an areal capacity of 6.83 mA h cm<sup>-2</sup>. These results illustrate that organic compounds coated onto a carbonaceous template can form structures that function as redox mediators and S-hosts in Li–S batteries, which highlights the potential for such Li–S batteries to be used as advanced high-energy-density energy-storage systems.

## 4. Experimental Section

**Materials:** All chemicals were purchased from Sigma-Aldrich or Alfa Aesar, and were dried before use. 1-Pentanol was distilled from sodium under reduced pressure. *N,N'*-dimethylformamide (DMF) was purified using a PureSolv solvent-purification system (Inert Corp., USA). 4-Nitrophthalonitrile (99%), TEG (99%), potassium carbonate (K<sub>2</sub>CO<sub>3</sub>, anhydrous, 99.9%), Co(OAc)<sub>2</sub>·4(H<sub>2</sub>O), 99.999% trace metals basis), 1,8-diazabicyclo[5.4.0]undec-7-ene (DBU, 98%), *N*-methyl-2-pyrrolidinone (NMP, ≥99.5%), ethylene carbonate (anhydrous, ≥99%).

**Preparation of Bisphthalonitrile TEG-Pn Dimer:** 4-Nitrophthalonitrile (2.00 g, 11.6 mmol) and TEG (826 mg, 5.5 mmol) were dissolved in DMF (10 mL). The resulting solution was treated with K<sub>2</sub>CO<sub>3</sub> (1.67 g, 12.1 mmol) and then stirred at 50 °C for 72 h. The resulting mixture was treated with deionized water (DI water, 200 mL) and then stirred at room temperature for 1 h to afford a precipitate, which was filtered and washed successively with DI water (200 mL) and ethanol (200 mL). The filtered powder was refluxed in ethanol (150 mL) for 6 h, and filtered after recrystallization at room temperature. The solid was further dried in a vacuum oven at 60 °C for 12 h to afford an ivory powder (1.40 g, 63.2%). <sup>1</sup>H NMR (300 MHz, DMSO, δ): 8.03 (dd, *J* = 1.8 Hz, 2 H, ArH), 7.75 (d, *J* = 2.7 Hz, 2 H, ArH), 7.45 (dd, *J* = 2.7, 6.3 Hz, 2 H, ArH), 4.27 (t, *J* = 4.5 Hz, 4 H, OCH<sub>2</sub>), 3.77 (t, *J* = 4.5 Hz, 4 H, OCH<sub>2</sub>), 3.59 (s, 4 H, CH<sub>2</sub>). <sup>13</sup>C[<sup>1</sup>H] NMR (500 MHz, DMSO-*d*<sub>6</sub>, δ): 162.4, 136.2, 120.8, 120.6, 116.8, 116.7, 116.2, 106.5, 70.4, 69.1, and 69.0.

**Preparation of TCP, TCP/MC, and S@TCP/MC:** As-prepared TEG-Pn dimer (800 mg) and Co(OAc)<sub>2</sub>·4(H<sub>2</sub>O) (200 mg) were dissolved in a mixture of 1-pentanol and DMF (3:1 v/v, 20 mL) at 80 °C. At this stage, for the preparation of TCP/MCs, MCs (1 or 3 equivalents by mass) were added to this solution. Homopolymerized TCP was prepared without the addition of MCs. The resulting solution (without or with MCs added) was treated with DBU (1 mL) and then stirred at 160 °C for 16 h. The resulting mixture was centrifuged at 8000 rpm for 5 min to collect the precipitate, which was then successively washed with DI water, ethanol, DMF and acetone, and finally dried under reduced pressure at 60 °C for 24 h. The resulting solid was annealed at 250 °C for 2 h at a heating rate of 5 °C min<sup>-1</sup> under a flow of Ar (50 sccm). As-prepared TCP/MCs was mixed with sulfur in the weight ratio of 1:3. The mixture was ground using a mortar for 1 h at room temperature and then was heated at 155 °C for 12 h in a Teflon liner under an Ar atmosphere to obtain the S@TCP/MCs.

**Material Characterizations:** Morphologies of samples were determined by field-emission scanning electron microscopy (MERLIN, Carl Zeiss) and TEM (Libra 200 HT Mc Cs, 200 kV). Structural properties of samples were determined by UV–vis spectroscopy (UV-2600, Shimadzu) and FTIR spectroscopy (Bruker IFS-66/S, TENSOR27). Raman spectroscopy was performed using an inVia Raman microscope to confirm the structural properties of samples. XPS (Thermo Fisher ESCALAB 250Xi) was performed to probe the surface electronic states and elemental composition of samples. Thermogravimetric analysis (TGA, Seiko Exstar 6000, TG/DTA6100) curves were measured at a heating rate of 10 °C min<sup>-1</sup> in N<sub>2</sub> gas.

**Electrochemical Measurements:** TCP/MCs electrodes were prepared by suspending TCP/MCs powder (80 wt%), carbon black (a conductive additive; 10 wt%), and polyvinylidene difluoride (PVDF; a binder; 10 wt%) in NMP. The resulting slurry was coated onto aluminum foil to given an S-loading area of 1.5 mg cm<sup>-2</sup> (or 5.5 or 6.6 mg cm<sup>-2</sup> for high loading tests), and the resulting coated foil was dried in an oven

at 80 °C for 12 h. The above procedure was also used to prepare mTCP/MC and MC electrodes, which served as reference electrodes. Coin cells (CR2032) were assembled using the TCP/MC electrode, an Li-metal anode, a polypropylene separator (Celgard 2400), and an electrolyte composed of 1.0 M bis(trifluoromethane)sulfonimide lithium (Sigma-Aldrich) and 0.3 M lithium nitrate (Sigma-Aldrich) in a 1:1 v/v mixture of 1,3-dioxolane (Sigma-Aldrich) and 1,2-dimethoxyethane (Sigma-Aldrich). Ten milliliters of electrolyte (E) were added per milligram of S (E/S ratio = 10). CV profiles were measured at scan rates from 0.1 to 0.8 mV s<sup>-1</sup> over the potential range of 1.7 to 2.8 V, and electrochemical impedance spectroscopy was performed within a frequency range of 0.01 to 1 × 10<sup>6</sup> Hz using a Bio-Logic instrument (VMP3 potentiostat/galvanostat). GCD profiles were measured at various Cs (0.1, 0.2, 0.5, 1.0, 2.0, 3.0, 4.0, and 5.0) to determine rate performance and at 0.2 and 1.0 C to determine cycle performance using a Maccor Series 400 automated test system (where 1 C = 1675 mA h g<sup>-1</sup>). The pouch-type cells were assembled using a S@TCP cathode (30 mm × 30 mm) paired with 50 μm Li coated on the Cu foil as anode (35 mm × 35 mm). The electrodes containing a PP separator (40 mm × 40 mm) were sealed in an Al pouch while filing the 1.0 M LiTFSI in a 1:1 v/v mixture of 1,3-dioxolane and 1,2-dimethoxyethane with 0.3 M LiNO<sub>3</sub> in a dry room with the dew point (less than -70 °C). After resting further for 24 h, the pouch cells were cycled at 30 °C oven in the voltage range of 1.7–2.8 V at 0.1C.

**Computational Details:** DFT calculations were performed in the Vienna Ab initio Simulation Package (VASP).<sup>[37]</sup> Projector-augmented wave (PAW) pseudopotentials<sup>[38]</sup> with a plane-wave basis set were implemented in the VASP. Perdew–Burke–Ernzerhof parametrization of the generalized gradient approximation (GGA)<sup>[39]</sup> was used for the exchange-correlation functional. A 1 × 1 × 2 *k*-point grid was used to calculate the TCP molecule. The DFT-D3 correction method<sup>[40]</sup> was used for accurate calculations of the van der Waals interactions between LiPS and substrate. The generalized gradient approximation + U method<sup>[41]</sup> was adopted to address the localization of the *d* orbital in Co ions in TCP (with a *U* value of 2.0 eV), as employed in a previous study.<sup>[42]</sup> A kinetic energy cutoff of 500 eV was used in all of the calculations, and all of the structures were optimized until the force in the unit cell converged to within 0.03 eV Å<sup>-1</sup>.

**Li<sub>2</sub>S<sub>6</sub> Symmetric Cell Test:** Electrodes were fabricated by mixing S-free TCP/MCs (80 wt%), carbon black (10 wt%), and PVDF binder (10 wt%) in NMP. The resulting slurry was coated onto aluminum foil, and the resulting coating was dried in an oven at 80 °C for 12 h. Two of these electrodes were each treated with 30 μL 0.5 M Li<sub>2</sub>S<sub>6</sub> to afford symmetric cells, which were then analyzed by CV at various scan rates (0.2, 0.5, 1.0, and 2.0 mV s<sup>-1</sup>) over the potential range of -1.0 to 1.0 V.

**Li<sub>2</sub>S Precipitation Measurements:** S-free electrodes fabricated as above were treated with 30 μL of 0.5 M Li<sub>2</sub>S<sub>8</sub> containing E on the cathode site, and with 30 μL of 0.5 M Li<sub>2</sub>S<sub>8</sub>-free E on the anode site, to form a symmetric cell. The resulting cells were first discharged galvanostatically to 2.11 V at 0.05 C and then discharged potentiostatically at 2.10 V for Li<sub>2</sub>S nucleation and growth.

## Supporting Information

Supporting Information is available from the Wiley Online Library or from the author.

## Acknowledgements

Y.K. and W.K. contributed equally to this work. This work is financially supported by the National Research Foundation of Korea (NRF) grant funded by the Korea government (No. 2021M3D1A2043791) and SKKU Global Research Platform Research Fund, Sungkyunkwan University, 2022. Y.K. was supported by Korea Initiative for fostering University of Research and Innovation Program of the National Research

Foundation (NRF) funded by the Korean government (MSIT) (No. 2020M3H1A1A077095). J.L. gratefully acknowledges the financial supports from the Hong Kong Polytechnic University (1-BD40).

## Conflict of Interest

The authors declare no conflict of interest.

## Data Availability Statement

The data that support the findings of this study are available from the corresponding author upon reasonable request.

## Keywords

coordination chemistry, lithium–sulfur batteries, molecular design, polymeric phthalocyanine, redox mediators

Received: December 22, 2022

Revised: March 6, 2023

Published online: April 7, 2023

- [1] a) A. Manthiram, Y. Fu, S. H. Chung, C. Zu, Y. S. Su, *Chem. Rev.* **2014**, *114*, 11751; b) Z. W. Seh, Y. Sun, Q. Zhang, Y. Cui, *Chem. Soc. Rev.* **2016**, *45*, 5605; c) P. G. Bruce, S. A. Freunberger, L. J. Hardwick, J. M. Tarascon, *Nat. Mater.* **2011**, *11*, 19.
- [2] a) R. Fang, S. Zhao, Z. Sun, D. W. Wang, H. M. Cheng, F. Li, *Adv. Mater.* **2017**, *29*, 201606823; b) M. Wild, L. O'Neill, T. Zhang, R. Purkayastha, G. Minton, M. Marinescu, G. J. Offer, *Energy Environ. Sci.* **2015**, *8*, 3477; c) C. Dong, C. Zhou, Y. Li, Y. Yu, T. Zhao, G. Zhang, X. Chen, K. Yan, L. Mai, X. Xu, *Small* **2023**, *19*, 2205855.
- [3] a) H.-J. Peng, J.-Q. Huang, X.-B. Cheng, Q. Zhang, *Adv. Energy Mater.* **2017**, *7*, 1700260; b) X. Liu, J. Q. Huang, Q. Zhang, L. Mai, *Adv. Mater.* **2017**, *29*, 201601759; c) M. Jana, R. Xu, X.-B. Cheng, J. S. Yeon, J. M. Park, J.-Q. Huang, Q. Zhang, H. S. Park, *Energy Environ. Sci.* **2020**, *13*, 1049; d) C. Zhou, Z. Li, X. Xu, L. Mai, *Nat. Sci. Rev.* **2021**, *8*, nwab055.
- [4] a) M.-S. S. S.-C. Han, H. Lee, H.-S. Kim, H.-J. Ahn, A. J.-Y. Lee, *J. Electrochem. Soc.* **2003**, *150*, A889; b) L. Ji, M. Rao, S. Aloni, L. Wang, E. J. Cairns, Y. Zhang, *Energy Environ. Sci.* **2011**, *4*, 5053; c) Q. Liu, X. Han, Z. Zheng, P. Xiong, R. G. Jeong, G. Kim, H. Park, J. Kim, B. K. Kim, H. S. Park, *Adv. Funct. Mater.* **2022**, *32*, 2207094; d) J. Ruan, H. Sun, Y. Song, Y. Pang, J. Yang, D. Sun, S. Zheng, *Energy Mater.* **2022**, *1*, 100018.
- [5] a) H. Wang, Y. Yang, Y. Liang, J. T. Robinson, Y. Li, A. Jackson, Y. Cui, H. Dai, *Nano Lett.* **2011**, *11*, 2644; b) J. S. Yeon, S. Yun, J. M. Park, H. S. Park, *ACS Nano* **2019**, *13*, 5163; c) J. S. Yeon, Y. H. Ko, T. H. Park, H. Park, J. Kim, H. S. Park, *Energy Environ. Mater.* **2021**, *5*, 555.
- [6] a) C. Liang, N. J. Dudney, J. Y. Howe, *Chem. Mater.* **2009**, *21*, 4724; b) C. Ye, L. Zhang, C. Guo, D. Li, A. Vasileff, H. Wang, S. Z. Qiao, *Adv. Funct. Mater.* **2017**, *27*, 1702524; c) J. S. Yeon, S. H. Park, J. Suk, H. Lee, H. S. Park, *Chem. Eng. J.* **2020**, *382*, 122946; d) S. Zheng, F. Yi, Z. Li, Y. Zhu, Y. Xu, C. Luo, J. Yang, C. Wang, *Adv. Funct. Mater.* **2014**, *24*, 4156.
- [7] a) J. He, A. Bhargava, A. Manthiram, *Adv. Energy Mater.* **2021**, *12*, 2103204; b) H. Shi, X. Ren, J. Lu, C. Dong, J. Liu, Q. Yang, J. Chen, Z. S. Wu, *Adv. Energy Mater.* **2020**, *10*, 200227; c) Z. Bian, Y. Xu, T. Yuan, C. Peng, Y. Pang, J. Yang, S. Zheng, *Batteries Supercaps* **2019**, *2*, 560.
- [8] a) B. Yu, A. Huang, D. Chen, K. Srinivas, X. Zhang, X. Wang, B. Wang, F. Ma, C. Liu, W. Zhang, J. He, Z. Wang, Y. Chen, *Small* **2021**, *17*, e2100460; b) D. Liu, C. Zhang, G. Zhou, W. Lv, G. Ling, L. Zhi, Q. H. Yang, *Adv. Sci. (Weinh)* **2018**, *5*, 1700270.
- [9] Q. H. Nguyen, V. T. Luu, S. N. Lim, Y. W. Lee, Y. Cho, Y. S. Jun, M. H. Seo, W. Ahn, *ACS Appl. Mater. Interfaces* **2021**, *13*, 28036.
- [10] a) X. Li, X. Yang, J. Ye, G. Xia, Z. Fu, C. Hu, *Chem. Eng. J.* **2021**, *405*, 126947; b) X. X. Yang, W. Z. Du, X. T. Li, Y. Zhang, Z. Qian, M. J. Biggs, C. Hu, *ChemSusChem* **2020**, *13*, 3034; c) X. X. Yang, X. T. Li, C. F. Zhao, Z. H. Fu, Q. S. Zhang, C. Hu, *ACS Appl. Mater. Interfaces* **2020**, *12*, 32752.
- [11] a) T. Nakazono, N. Amino, R. Matsuda, D. Sugawara, T. Wada, *Chem. Commun. (Camb)* **2022**, *58*, 7674; b) M. Chevir, S. Lakshminpathi, *Chem. Phys. Lett.* **2020**, *739*, 136942.
- [12] Y. Kim, D. Kim, J. Lee, L. Y. S. Lee, D. K. P. Ng, *Adv. Funct. Mater.* **2021**, *31*, 2103290.
- [13] a) Y. Liang, Z. Tao, J. Chen, *Adv. Energy Mater.* **2012**, *2*, 742; b) S. Muench, A. Wild, C. Friebe, B. Haupler, T. Janoschka, U. S. Schubert, *Chem. Rev.* **2016**, *116*, 9438.
- [14] M. Zheng, Y. Chi, Q. Hu, H. Tang, X. Jiang, L. Zhang, S. Zhang, H. Pang, Q. Xu, *J. Mater. Chem. A* **2019**, *7*, 17204.
- [15] J. Lee, Y. Kim, S. Park, K. H. Shin, G. Jang, M. J. Hwang, D. Kim, K. A. Min, H. S. Park, B. Han, D. K. P. Ng, L. Y. S. Lee, *Energy Environ. Mater.* **2022**, e12468.
- [16] a) J. Su, J.-J. Zhang, J. Chen, Y. Song, L. Huang, M. Zhu, B. I. Yakobson, B. Z. Tang, R. Ye, *Energy Environ. Sci.* **2021**, *14*, 483; b) P. Alessio, M. L. Rodriguez-Mendez, J. A. De Saja Saez, C. J. Constantino, *Phys. Chem. Chem. Phys.* **2010**, *12*, 3972.
- [17] a) L. Xu, Q. Jiang, Z. Xiao, X. Li, J. Huo, S. Wang, L. Dai, *Angew. Chem., Int. Ed. Engl.* **2016**, *55*, 5277; b) Y. Men, P. Li, J. Zhou, G. Cheng, S. Chen, W. Luo, *ACS Catal.* **2019**, *9*, 3744; c) L. Chen, Y. Zhang, H. Wang, Y. Wang, D. Li, C. Duan, *Nanoscale* **2018**, *10*, 21019.
- [18] a) Y. Wang, N. Hu, Z. Zhou, D. Xu, Z. Wang, Z. Yang, H. Wei, E. S.-W. Kong, Y. Zhang, *J. Mater. Chem.* **2011**, *21*, 3779; b) Y. Xia, S. Kashtanov, P. Yu, L.-Y. Chang, K. Feng, J. Zhong, J. Guo, X. Sun, *Nano Energy* **2020**, *67*, 104163; c) I. S. Kwon, I. H. Kwak, J. Y. Kim, H. G. Abbas, T. T. Debela, J. Seo, M. K. Cho, J. P. Ahn, J. Park, H. S. Kang, *Nanoscale* **2019**, *11*, 14266.
- [19] a) X. Hu, S. Zhang, J. Sun, L. Yu, X. Qian, R. Hu, Y. Wang, H. Zhao, J. Zhu, *Nano Energy* **2019**, *56*, 109; b) G. Greczynski, L. Hultman, *Sci. Rep.* **2021**, *11*, 11195.
- [20] a) W. Gu, M. Sevilla, A. Magasinski, A. B. Fuertes, G. Yushin, *Energy Environ. Sci.* **2013**, *6*, 2465; b) D. G. de Oteyza, A. El-Sayed, J. M. Garcia-Lastra, E. Gori, T. N. Krauss, A. Turak, E. Barrena, H. Dosch, J. Zegenhagen, A. Rubio, Y. Wakayama, J. E. Ortega, *J. Chem. Phys.* **2010**, *133*, 214703; c) M. Wang, J. Han, Y. Hu, R. Guo, *RSC Adv.* **2017**, *7*, 15513.
- [21] a) K. Han, J. Shen, S. Hao, H. Ye, C. Wolverton, M. C. Kung, H. H. Kung, *ChemSusChem* **2014**, *7*, 2545; b) G. Zhou, Y. Zhao, C. Zu, A. Manthiram, *Nano Energy* **2015**, *12*, 240.
- [22] a) X. Tao, J. Wang, C. Liu, H. Wang, H. Yao, G. Zheng, Z. W. Seh, Q. Cai, W. Li, G. Zhou, C. Zu, Y. Cui, *Nat. Commun.* **2016**, *7*, 11203; b) Z. Sun, J. Zhang, L. Yin, G. Hu, R. Fang, H.-M. Cheng, F. Li, *Nat. Commun.* **2017**, *8*, 14627.
- [23] a) B. Häupler, A. Wild, U. S. Schubert, *Adv. Energy Mater.* **2015**, *5*, 1402034; b) Y. Lu, J. Chen, *Nat. Rev. Chem.* **2020**, *4*, 127.
- [24] a) L. Kong, J.-X. Chen, H.-J. Peng, J.-Q. Huang, W. Zhu, Q. Jin, B.-Q. Li, X.-T. Zhang, Q. Zhang, *Energy Environ. Sci.* **2019**, *12*, 2976; b) Y. Song, Z. Sun, Z. Fan, W. Cai, Y. Shao, G. Sheng, M. Wang, L. Song, Z. Liu, Q. Zhang, J. Sun, *Nano Energy* **2020**, *70*, 104555.
- [25] a) F. Y. Fan, W. C. Carter, Y. M. Chiang, *Adv. Mater.* **2015**, *27*, 5203; b) Z. Li, Y. Zhou, Y. Wang, Y.-C. Lu, *Adv. Energy Mater.* **2019**, *9*, 1802207.

- [26] J. Lei, X. X. Fan, T. Liu, P. Xu, Q. Hou, K. Li, R. M. Yuan, M. S. Zheng, Q. F. Dong, J. J. Chen, *Nat. Commun.* **2022**, *13*, 202.
- [27] a) Y. Tian, G. Li, Y. Zhang, D. Luo, X. Wang, Y. Zhao, H. Liu, P. Ji, X. Du, J. Li, Z. Chen, *Adv. Mater.* **2020**, *32*, 1904876; b) Z. A. Ghazi, X. He, A. M. Khattak, N. A. Khan, B. Liang, A. Iqbal, J. Wang, H. Sin, L. Li, Z. Tang, *Adv. Mater.* **2017**, *29*, 1606817.
- [28] B. Yin, S. Liang, D. Yu, B. Cheng, I. L. Egun, J. Lin, X. Xie, H. Shao, H. He, A. Pan, *Adv. Mater.* **2021**, *33*, 2100808.
- [29] X. Zhou, R. Meng, N. Zhong, S. Yin, G. Ma, X. Liang, *Small Methods* **2021**, *5*, 2100571.
- [30] X. Yang, A. L. Rogach, *Adv. Energy Mater.* **2019**, *9*, 1900747.
- [31] Y. S. Lee, K. S. Ryu, *Sci. Rep.* **2017**, *7*, 16617.
- [32] a) W. Chen, Y. Hu, W. Lv, T. Lei, X. Wang, Z. Li, M. Zhang, J. Huang, X. Du, Y. Yan, W. He, C. Liu, M. Liao, W. Zhang, J. Xiong, C. Yan, *Nat. Commun.* **2019**, *10*, 4973; b) X. Zhang, Y. Chen, F. Ma, X. Chen, B. Wang, Q. Wu, Z. Zhang, D. Liu, W. Zhang, J. He, Z.-L. Xu, *Chem. Eng. J.* **2022**, *436*, 134945.
- [33] a) Z. Chang, H. Dou, B. Ding, J. Wang, Y. Wang, X. Hao, D. R. MacFarlane, *J. Mater. Chem. A* **2017**, *5*, 250; b) W. Huang, Z. Lin, H. Liu, R. Na, J. Tian, Z. Shan, *J. Mater. Chem. A* **2018**, *6*, 17132; c) X. Chen, X. Ding, C. Wang, Z. Feng, L. Xu, X. Gao, Y. Zhai, D. Wang, *Nanoscale* **2018**, *10*, 13694.
- [34] X. Hong, J. Jin, T. Wu, Y. Lu, S. Zhang, C. Chen, Z. Wen, *J. Mater. Chem. A* **2017**, *5*, 14775.
- [35] A. Liu, G. Liu, C. Zhu, H. Zhu, E. Fortunato, R. Martins, F. Shan, *Adv. Electron. Mater.* **2016**, *2*, 1600140.
- [36] a) X. Li, C. Shao, X. Wang, J. Wang, G. Liu, W. Yu, X. Dong, J. Wang, *Chem. Eng. J.* **2022**, *446*, 137530; b) S. H. Chung, A. Manthiram, *Adv. Mater.* **2014**, *26*, 7352.
- [37] G. Kresse, J. Furthmüller, *Comput. Mater. Sci.* **1996**, *6*, 15.
- [38] P. E. Blochl, O. Jepsen, O. K. Andersen, *Phys. Rev. B: Condens. Matter* **1994**, *49*, 16223.
- [39] K. B. John, P. Perdew, M. Ernzerhof, *Phys. Rev. Lett.* **1996**, *77*, 3865.
- [40] S. Grimme, J. Antony, S. Ehrlich, H. Krieg, *J. Chem. Phys.* **2010**, *132*, 154104.
- [41] V. I. Anisimov, F. Aryasetiawan, A. I. Lichtenstein, *J. Phys. Condens. Matter* **1997**, *9*, 767.
- [42] Y. Wang, X. Li, J. Yang, *Phys. Chem. Chem. Phys.* **2019**, *21*, 5424.